Postweld Heat Treatment on Toughness of Electric-Resistance Welded X70 Steel

The effect of peak temperatures during PWHT on impact toughness at low temperatures of HF-ERW X70 pipeline welds is investigated.

BY K. RAVIKIRAN, L. LI, N. K. SHARMA, N. ANDERSON, Y. WANG, S. D. CHOUDHURY, N. SAINI, AND M. RASHID

Abstract

The effect of postweld heat treatment (PWHT) on Charpy V-notch impact toughness of a high-frequency electric-resistance welded (HF-ERW) grade X70 pipeline steel is investigated. PWHT thermal cycles are simulated using the Gleeble on the as-welded specimens. Microstructure, along with crystallographic texture and microhardness, is characterized in specimens that are impact tested at −5°C (23°F), −30°C (−22°F), and −45°C (−49°F). The impact toughness values show a wide scatter band and decrease with the increasing peak temperature of the PWHT. For higher peak temperatures, the microstructure of the heat-affected zone (HAZ) gradually changed from equiaxed ferrite to bainitic ferrite. Furthermore, the prior austenite grain size (PAGS) increases with the increasing peak temperature. The density of high-angle grain boundaries decreases, and the fraction of cleavage planes {100} parallel to the impact fracture plane increases for higher peak temperatures of the PWHT.

Keywords

- X70 Steel
- ERW
- Microstructure
- Postweld Heat Treatment
- Impact Toughness

Introduction

Longitudinal seam welded linepipe manufactured by high-frequency electric resistance welding (HF-ERW) is widely used to transport oil and natural gas products (Refs. 1, 2). In HF-ERW, a thermomechanically processed steel strip is cold-formed into a cylindrical shape. The abutting edges of the strip are joined by a combination of localized resistance heating and mechanical upset (Ref. 3). Figure 1 shows an example of the longitudinal seam welded HF-ERW joint.

Unlike other resistance welding methods, the high-frequency heat will be concentrated in a narrow region due to the skin effect of induced currents (Ref. 5). Furthermore, heat is concentrated at the outer and inner diameters of the strip edges (Ref. 6), resulting in a smaller width of heat heat-affected zone (HAZ) in the middle thickness as compared to the outer diameter and inner diameter surfaces of the pipe, leading to an hourglass-shaped HAZ (Fig. 1) (Ref. 5). Once the edges are heated, upsetting force (the "squeeze") is applied to join the strip edges to form a weld joint that is usually referred to as the bondline (Ref. 7). The molten metal mixed with slag is expelled from the faying surfaces as a flash during the upsetting. After welding, the joint is sprayed with water for cooling, and the flash is removed from the pipe surfaces (Ref. 3).

The rapid heating and cooling rates during the HF-ERW result in detrimental microstructural constituents, residual stresses, and poor mechanical properties (Refs. 6, 8–10). It is widely reported that the impact toughness at the bondline in the as-welded condition is lower than in the original steel strip (Refs. 6, 8, 9, 11, 12). In addition, high cooling rates may produce severe segregation of the alloying elements in the heat-affected zone (HAZ) (Ref. 13). Sharma et al. (Ref. 13) measured the alloying concentrations in the as-welded HAZ region by atom tomography. An increase in the concentration of carbon and manganese at the austenite and ferrite interface was observed, which suggests a negligible partitioning local equilibrium. Therefore, HF-ERW pipeline steel welds require a postweld heat treatment (PWHT) (Refs. 6, 8, 9, 12, 14–16) to homogenize the alloying elements, temper the brittle weld microstructure, reduce residual stresses, and recover the mechanical properties.

The most widely used PWHT is a normalizing cycle, which involves heating the weld joint to above the upper critical temperature (A_{e3}), followed by air cooling (Refs. 6, 10, 12).

https://doi.org/10.29391/2024.103.017

Zhang et al. (Ref. 10) reported that after the PWHT, the toughness was affected by both the microstructure and crystallographic texture. Chung et al. (Ref. 15) investigated the effect of two different PWHT cycles, one-step normalizing, and two-step quenching and tempering, on the impact toughness of X65-grade steel. Their results indicated that the PWHT improved the toughness compared to the as-welded condition; however, the toughness values were reduced to below the acceptance level as the impact test temperature was lowered (Ref. 15). Yan et al. (Ref. 8) indicated that the density of cleavage planes oriented for easy (i.e., cleavage) fracture was the primary cause of the toughness reduction in HF-ERW X65 steel line pipes after normalizing. They also suggested that the weld defects and large grain sizes after PWHT were the reasons for the poor toughness performance (Refs. 8, 10). Although the reasons for the toughness reduction were analyzed in detail, an effective method to improve the toughness of the welds was not given (Ref. 8). Khalaj et al. (Ref. 12) varied the finish cooling rates and temperatures for PWHT and observed the impact toughness of the X60 pipeline steel. They identified that a two-step quenching followed by tempering provided better mechanical properties than one-step normalizing. However, novel PWHT cycles during the manufacturing of HF-ERW pipe were not widely adopted

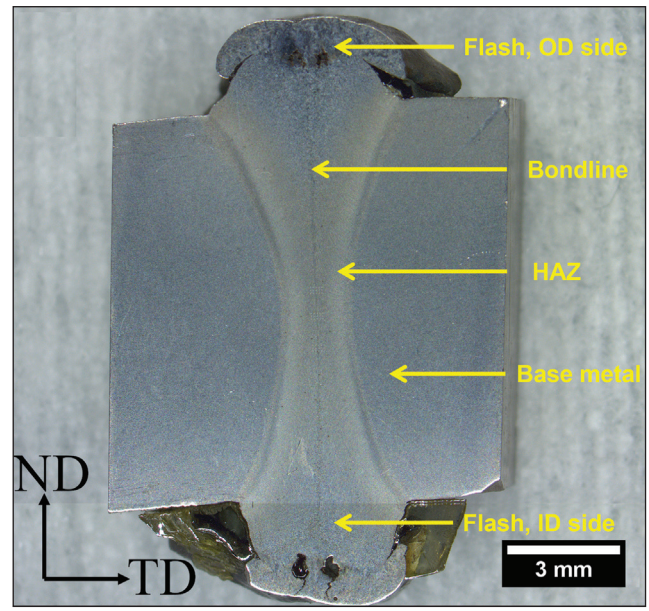

Fig. 1 — A HF-ERW joint in the as-welded condition with the typical hourglass-shaped heat-affected zone, bondline, flash, and base metal (Ref. 4).

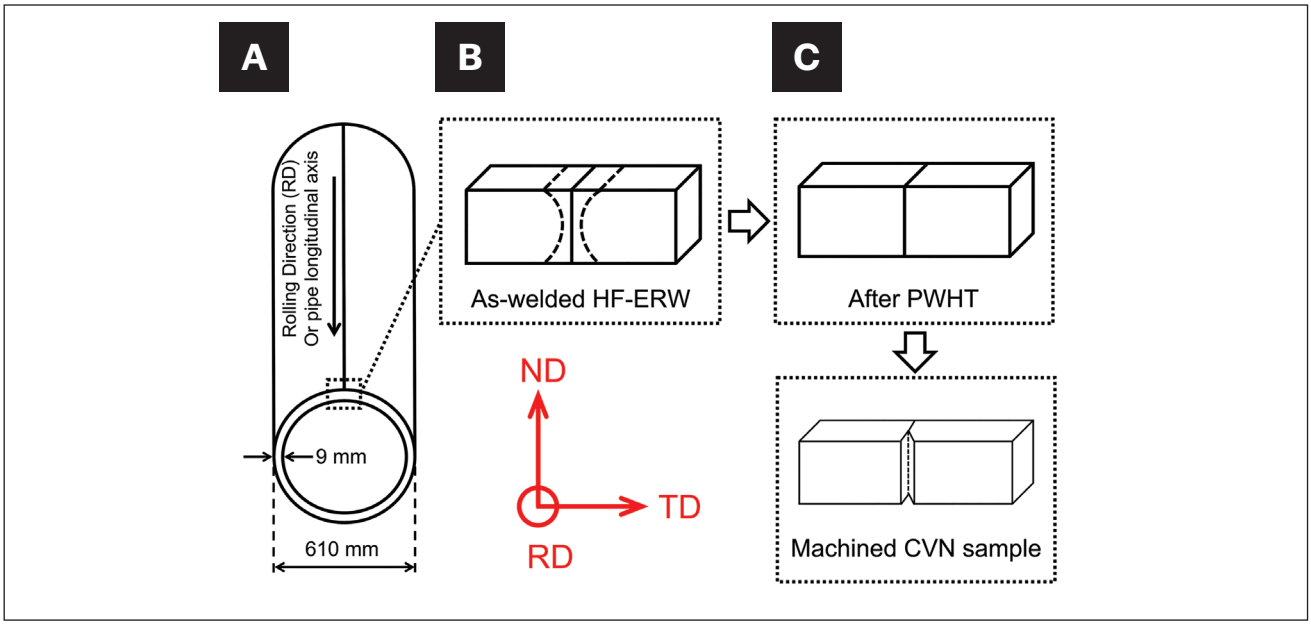

Fig. 2 — Schematic diagram of: A — HF-ERW pipe with steel processing directions; B — as-welded sample with typical hourglass shape and bondline; C — sample after PWHT showing bondline; D — CVN specimen with notch machined at the bondline. All dimensions are in millimeters. For referencing the specimen orientations against the pipe cross-section, ND refers to normal direction, TD refers to transverse direction, and RD refers to rolling direction.

Table 1 — Chemical Composition of X70-grade Base Metal Used in This Study

Element	C	Mn	Si	Nb	V+Ti	Cu+Ni+ Cr+ Mo	S+P
Wt-%	0.052	1.62	0.14	0.074	0.02	0.76	0.018

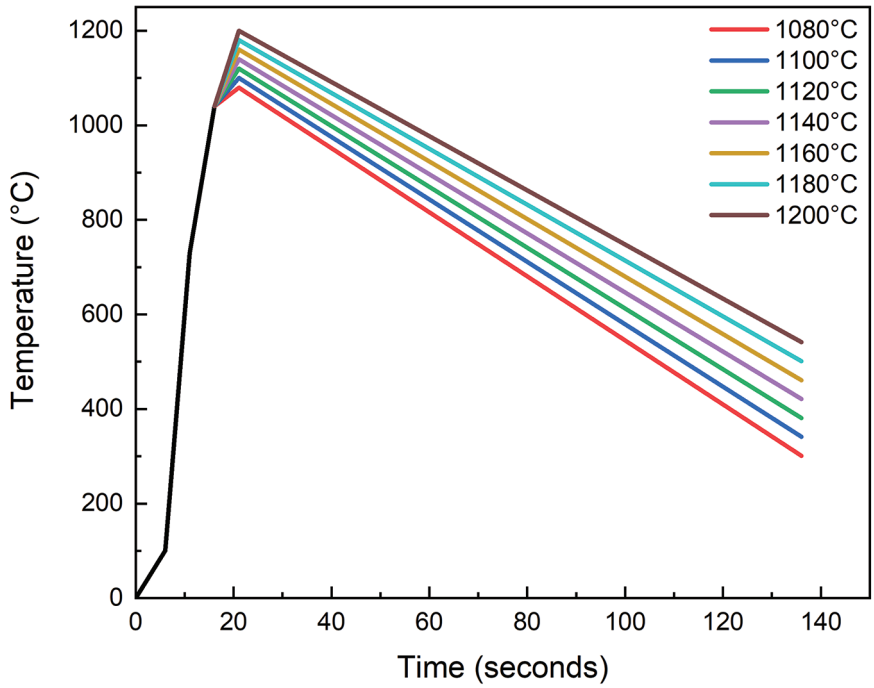

Fig. 3 — Schematic illustration of postweld heat treatment (PWHT) cycles on the Gleeble.

over conventional normalizing due to the lack of control over the PWHT process (Ref. 16).

In summary, toughness performance at low temperatures, such as –40°C (–40°F), is still low for HF-ERW pipe welds, and the mechanisms for the low toughness are not fully understood (Refs. 4, 6, 12), and therefore, no effective methods to improve the low-temperature toughness are available in the literature. It should be noted that the impact toughness of the HF-ERW pipeline steels is affected by many factors, including the alloy composition, welding parameters, and PWHT parameters (Refs. 8, 9, 12, 15). This work aims to study the effect of peak temperature during PWHT on the impact toughness at low temperatures of the HF-ERW X70 pipeline welds.

Experimental Procedures

The material used in the current study is X70-grade pipeline steel. The chemical composition is listed in Table 1.

The as-received HF-ERW pipe, with an outer diameter of 610 mm (24.016 in.) and a wall thickness of 9 mm (0.354 in.) (Fig. 2A), was initially production welded at the commercial pipe mill. Specimens for the postweld heat treatment (PWHT) were extracted from the as-welded pipe with 10 mm (0.394 in.) in the rolling direction (RD), 5 mm (0.197 in.) in the normal direction (ND), and 55 mm (2.165 in.) in the transverse direction (TD) (Fig. 2B).

The PWHT was then conducted using a Gleeble 3800 thermomechanical simulator. The details of the applied PWHT cycles are shown in Fig. 3. The simulation was performed by heating the sample to a desired peak temperature (T_p at 1080°C [1976°F], 1100°C [2012°F], 1120°C [2048°F], 1140°C [2084°F], 1160°C [2120°F], 1180°C [2156°F], and 1200°C [2192°F]) in a controlled heating rate: the heating intervals were 5 s in the 100–730°C (212–1346°F), 5 s in the 730–1040°C (1346–1904°F), and 5 s in the 1040-T_p°C. All the PWHTs were performed above A_{c3} temperature; a total of seven different peak temperatures, i.e., 1080°C, 1100°C, 1120°C, 1140°C, 1160°C, 1180°C, and 1200°C, were used for the PWHT. Following that, the specimens were cooled to room temperature at a constant linear cooling rate of 6.4°C (43°F)/s. These heating rates, hold times, and cooling rates were calculated from the production welding typical line speed and the typical length of the welded pipe in the PWHT furnaces.

After the PWHT, specimens were macro-etched to reveal the bondline (Fig. 2C), and V-notch was machined at the bondline (Fig. 2D) (Ref. 17). Charpy V-notch (CVN) impact testing was performed in accordance with ASTM A370, on the half-size specimens (10 mm × 5 mm × 55 mm), at –5°C (23°F), –30°C (–22°F), and –45°C (–49°F). It should be noted that ASTM A370 requires a minimum of three specimens to report the average values of the CVN test (Ref. 18). Although at each PWHT condition, more than three samples were tested, a few samples were discarded because the notch and crack propagation were not within ± 0.5 mm (0.020 in.) from the bondline. It is understood that the toughness is lowest within ± 0.5 mm from the bondline; therefore, samples that didn't meet this criterion were omitted (Ref. 17). Microhardness was

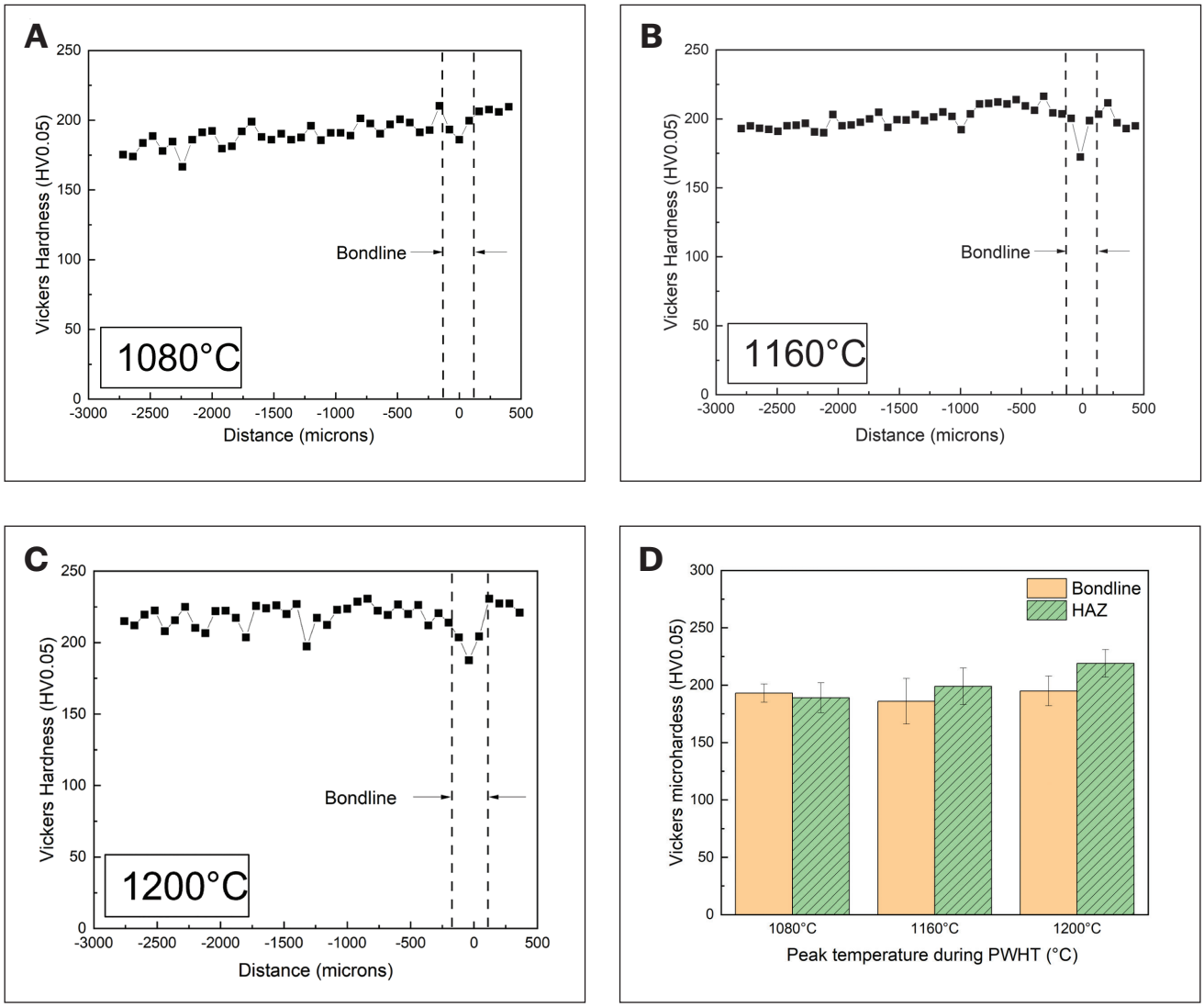

Fig. 4 — Microhardness distribution across the bondline for the samples PWHTed at: A — 1080°C; B — 1160°C; C — 1200°C. D — average microhardness values of the bondline and HAZ.

measured across the bondline using a Vickers microhardness tester according to ASTM E384 (Ref. 19). Measurements were taken with a 0.05 gf indentation load and 10 s dwell time at an interval of 60 µm. An average of three measurements were used at each location to represent the hardness.

For microstructure characterization, specimens were ground and polished using standard metallographic techniques. Etching was performed with 4 vol-% Nital (a mixture of alcohol and HNO_3). The microstructures were observed using an optical microscope and a field-emission scanning electron microscope (FESEM) equipped with energy dispersive spectroscopy (EDS). The SEM was operated in secondary electron (SE) mode using an in-lens detector. Imaging was performed at an accelerating voltage of 20 kV. During the investigation, the distance between the detector and the sample surface was ~10 mm. ImageJ software was used for the statistical analysis of microstructural constituents. Furthermore, electron backscattered diffraction (EBSD) map-

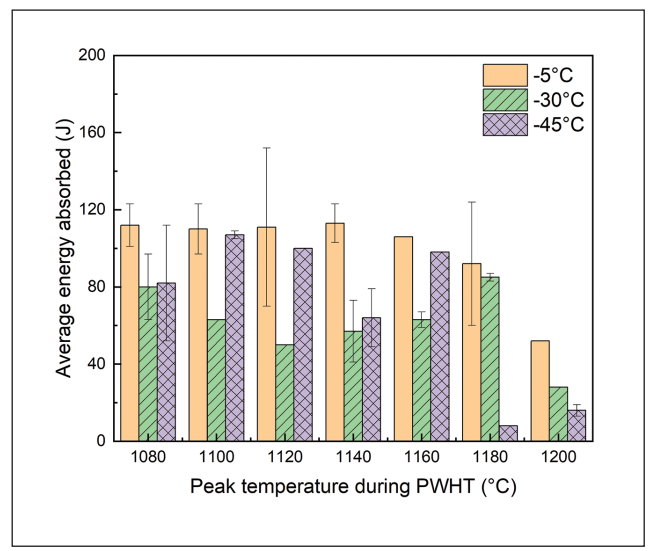

Fig. 5 — Average impact toughness testing results for the Gleeble simulated specimens with various peak temperatures and tested at –5°C, –30°C, and –45°C.

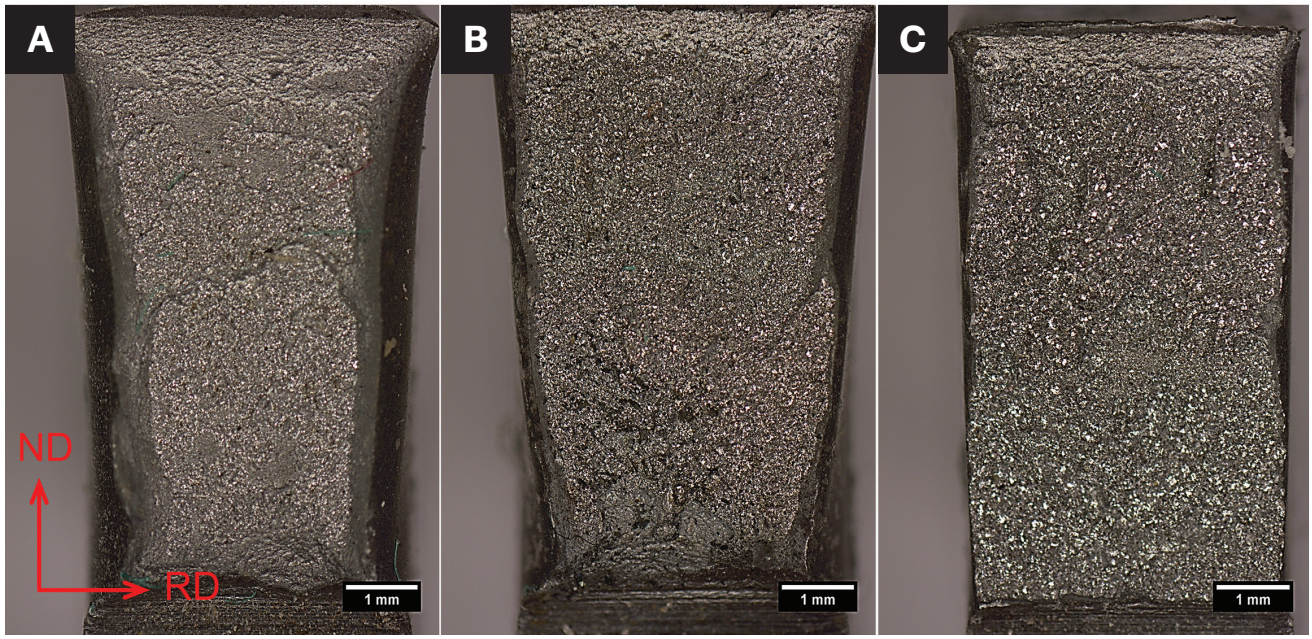

Fig. 6 — Fractography of samples PWHTed at: A — 1080°C; B — 1160°C; C — 1200°C and impact tested at -30°C.

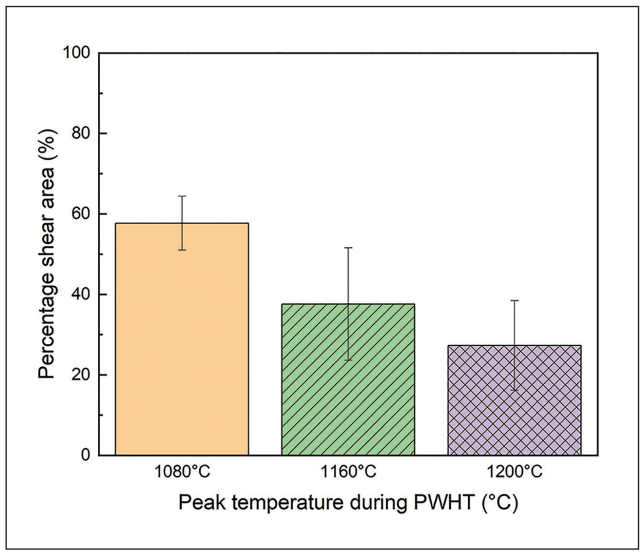

Fig. 7 — Percentage shear area (ductile fracture appearance) in specimens impact tested at –30°C, following PWHT at 1080°C, 1160°C, and 1200°C.

pings were acquired at an acceleration voltage of 20 kV, a tilt angle of 70 deg, and a step size between 0.25–0.5 µm.

Equilibrium phase fractions and critical temperatures (A_1, A_3, M_S, and B_S) for the X70 base metal used in the current study (Table 1) were calculated using Thermo-Calc on database TCFE10 (Ref. 20). Phase transformations occurring during the PWHT cycle were analyzed using the obtained dilatometry data from the Gleeble thermomechanical simulator. Transformation temperatures (A_{c1}, A_{c3}, A_{r1}, & A_{r3}) were determined by changes in slope as per ASTM A1033 (Ref. 21). The first-order derivative of dilation concerning temperature was taken and plotted versus temperature to accurately determine slope changes corresponding to phase changes, including minute changes associated with precipitates or other small volume fraction phases. Evidence of homogenization during the heating cycle of the PWHT was determined by deviations in the slope above A_{c3} on the dilation versus temperature plot, as shown in reference (Ref. 22).

Results

Figures 4A–C show the microhardness distribution across the bondline for the specimens PWHTed at peak temperatures of 1080°C, 1160°C, and 1200°C. The average microhardness values are summarized in Fig. 4E. It should be noted that the hardness distribution and microstructure for the sample PWHTed at 1080°C are the same as that of the sample PWHTed at 1100°C. Similarly, samples PWHTed at 1120°C, 1140°C, and 1160°C are the same, and 1180°C and 1200°C are comparable. Therefore, for brevity, the hardness and microstructure of the samples PWHTed at 1100°C, 1120°C, 1140°C, and 1180°C are not shown.

For the 1080°C peak temperature sample, the hardness at the bondline (193 ± 8 HV0.05) and hardness at the HAZ (189 ± 13 HV0.05) are similar (Fig. 4A). For the 1160°C peak temperature, the hardness at the bondline (186 ± 20 HV0.05) is like the 1080°C peak temperature sample (Fig. 4B). However, the HAZ has a relatively high hardness of 199 ± 16 HV0.05 (Fig. 4B). When the peak temperature for PWHT increases to 1200°C, the hardness at the bondline remains about 195 ± 13 HV0.05; however, there is a significant increase in hardness, to 219 ± 12 HV0.05, for the HAZ (Fig. 4C). It is apparent that the difference in hardness values between the bondline and the HAZ has increased with the increase in the peak temperature (Fig. 4D).

Results of the CVN impact toughness tests at –5°C, –30°C, and –45°C on specimens of different PWHT peak tempera-

Table 2 — Impact Energy of the Specimens Post-Weld Heat-treated at Different Peak Temperatures

Charpy V-notch Test Temperature (°C)	Peak Temperature for PWHT (°C)	Charpy V-notch Energy (J)	
		Individual Values	Average
-5	1080	116, 122, 113, 97	112 ± 11
	1100	104, 124, 101	110 ± 13
	1120	82, 140	111 ± 41
	1140	106, 120	113 ± 10
	1160	104, 108	106 ±3
	1180	70, 114	92 ± 32
	1200	52	52
-30	1080	60, 78, 78, 102	80 ± 17
	1100	63	63
	1120	50	50
	1140	72, 58, 40	57 ± 16
	1160	66, 60	63 ± 4
	1180	84, 87	85 ± 2
	1200	28	28
-45	1080	126, 52, 58, 82, 82	82 ± 30
	1100	104, 109	107 ± 2
	1120	84, 116	100 ±23
	1140	72, 64, 42, 76	64 ± 15
	1160	98	98
	1180	8	8
	1200	18, 14	16 ± 3

tures, i.e., 1080°C, 1100°C, 1120°C, 1140°C, 1160°C, 1180°C, and 1200°C, are shown Table 2. The average CVN values are collected for Fig. 5, which shows a sizeable statistical variation in the CVN values. However, a definite trend can be observed with the change in peak temperature. At each test temperature (–5°C, –30°C, and –45°C), the average energy absorbed shows a gradually decreasing trend as the peak temperature increases. For –5°C tests, the absorbed energy remains above 70J for all peak temperatures, except for 1200°C, whose specimens show 50J energy. For –30°C tests, the absorbed energy has decreased relative to the –5°C tests but remains above 40J, except for 1200°C, whose specimens show 25J energy. When tested at –45°C, the average absorbed energy has remained above 40J, except for 1180°C and 1200°C, whose specimens show single digits absorbed energy. Therefore, a significant drop in toughness has happened for the specimens PWHTed at peak temperatures of

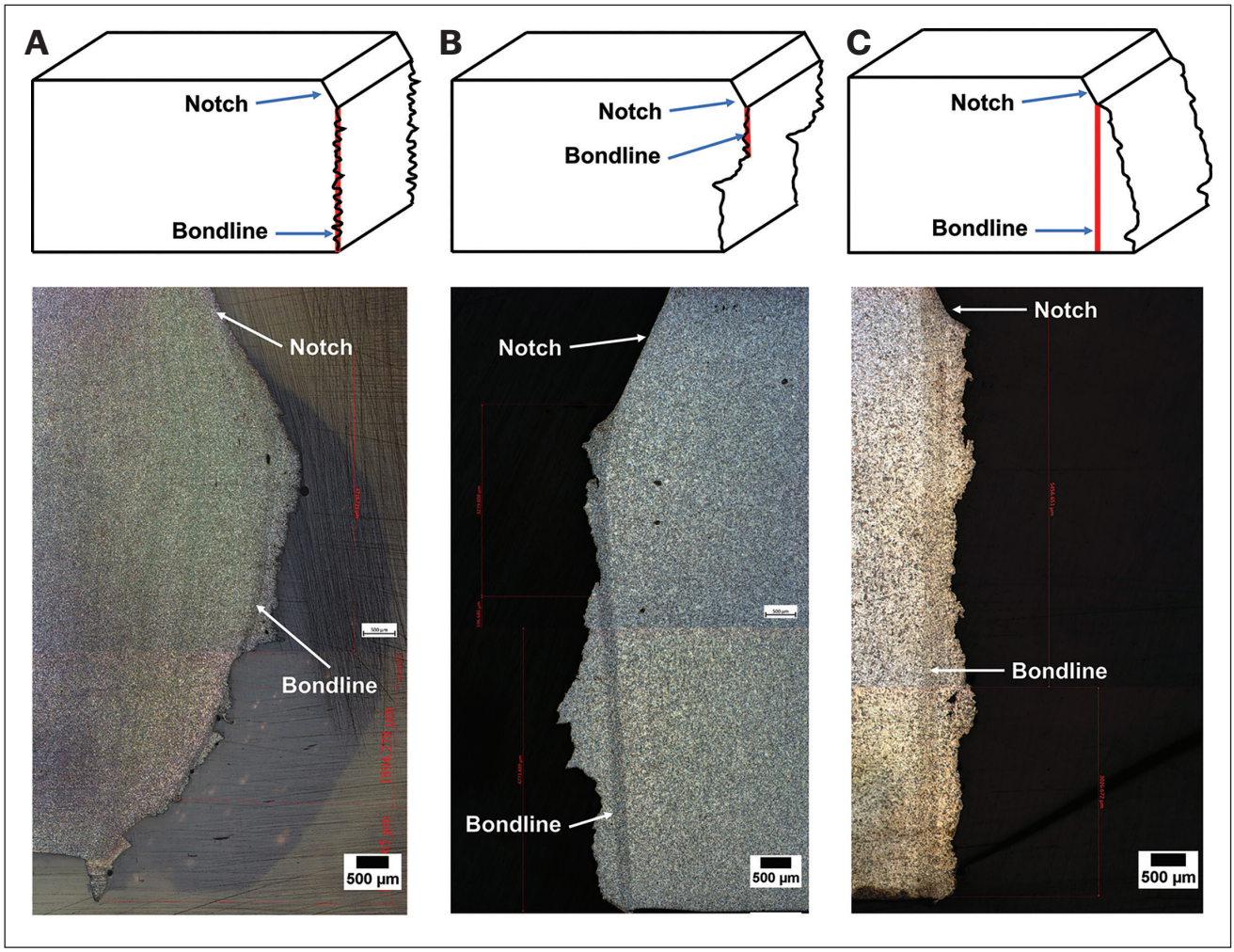

Fig. 8 — Schematic crack paths and representative micrographs for three typical crack paths observed in this study: A — Crack initiation and propagation are completely along the bondline; B — crack initiation is at the bondline, and propagates initially along the bondline, but deviates into the HAZ; C — the crack propagation is entirely contained in the HAZ.

1180°C and 1200°C, particularly for specimens tested at lower temperatures of −30°C and −45°C.

Figure 6 presents the representative fracture surfaces (in the ND-RD plane) for the samples PWHTed at 1080°C, 1160°C, and 1200°C and CVN tested at −30°C. The fracture surface shows some ductile (fibrous crack propagation) and brittle fracture regions. The ductile fracture region was observed along the four edges of the impact-tested samples. As shown in Fig. 7, the average value of the shear fracture percentage for the samples PWHTed at 1080°C, 1160°C, and 1200°C is 58 ± 7%, 38 ± 14%, and 27 ± 11%, respectively. The width of these ductile fracture bands has reduced with the increasing peak temperature for the PWHT.

Figure 8 shows the schematic and representative micrographs for three typical crack paths observed in this study. It was observed that the peak temperature has a strong correlation with the energy observed during impact testing and the crack propagation. As the peak temperature increased, most of the crack propagation shifted from the bondline to the heat-affected zone.

To correlate microstructure with crack propagation, electron backscattered diffraction (EBSD) is performed on the RD-TD surface. Figures 9-11 show the EBSD micrographs along the crack path in samples PWHTed at 1080°C, 1160°C, and 1200°C peak temperatures, and impact tested at −30°C. For lower peak temperatures, i.e., 1080°C, the crack initiation, and propagation are completely contained along the bondline. As the peak temperature for PWHT increased, such as to 1160°C, although the crack initiation is at the bondline, it shortly deviates into the HAZ (Fig. 9). Whereas, for the sample PWHTed at 1200°C, the crack propagation is entirely contained in the HAZ (Fig. 11). Therefore, it can be summarized that as the peak temperature increased, most of the crack propagation has shifted from the bondline to the HAZ. Among samples PWHTed at 1080°C, 1160°C, and 1200°C, both the prior austenite grain size (PAGS) and the ferrite grain size in the HAZ are finer for the sample with a peak temperature of 1080°C (Figs. 12-13). When the peak temperature has increased to 1200°C, there is a drastic increase in PAGS (Fig. 12) and ferrite grain size (Fig. 13) in the HAZ.

In body-centered cubic crystalline materials, especially at sub-zero temperatures, brittle fracture occurs on the {100}

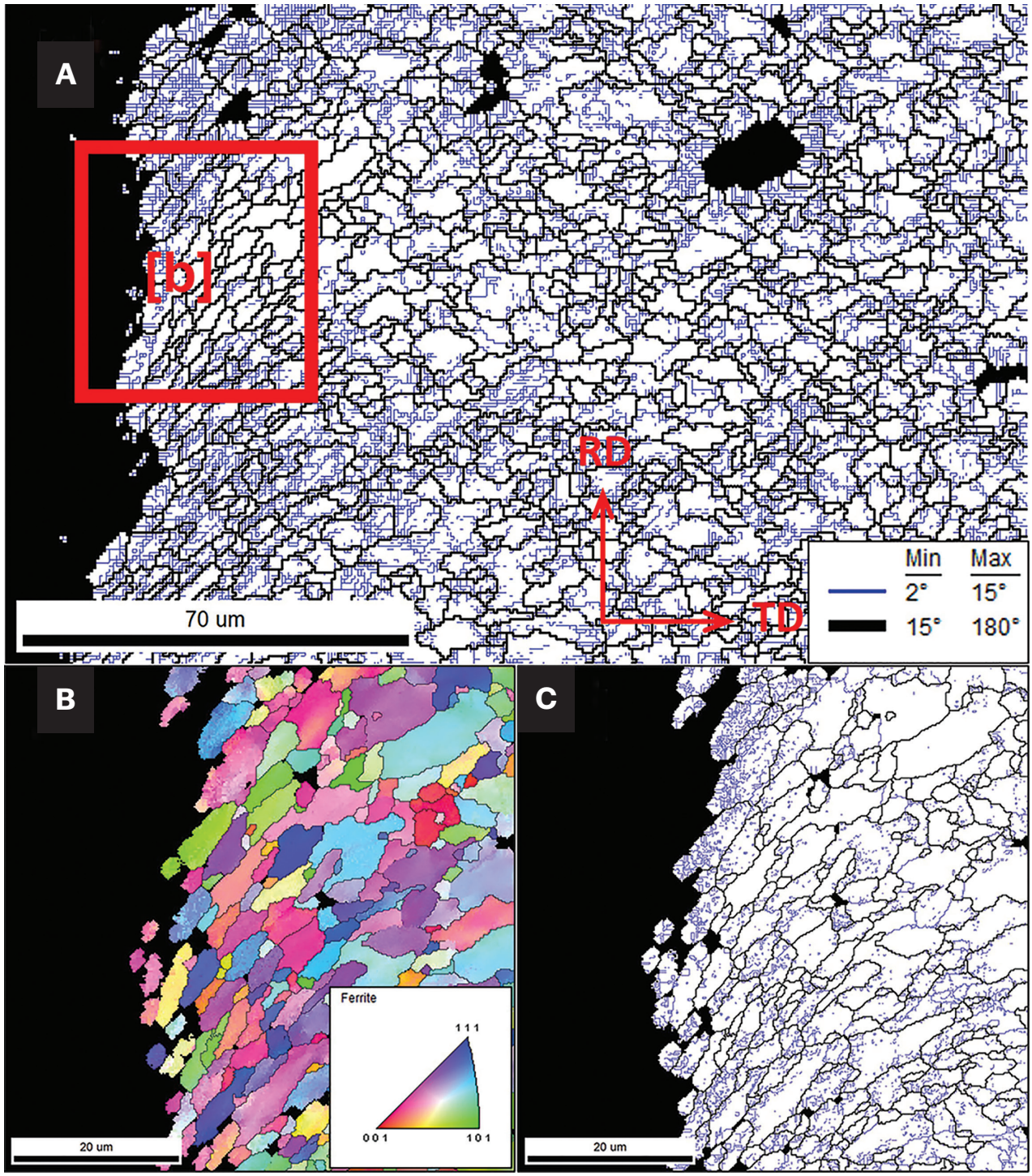

Fig. 9 — A — Grain boundary characteristics adjacent to fracture path for sample PWHTed at 1080°C, and CVN tested at –30°C; B — high magnification IPF image of the fracture path, which is along the bondline; C — is corresponding grain boundary characteristics.

cleavage planes. Therefore, the density of {100} cleavage planes on the fracture surface can significantly influence the impact toughness. The density of {100} cleavage planes in the HAZ that are within 10 deg of the actual fractured planes has been quantified based on the EBSD data. As shown in Fig. 14, with the increase in the peak temperature for the PWHT from 1080°C to 1200°C, there is an increase in the density of the {100} planes that are parallel to the fracture in the HAZ. Therefore, a positive correlation between the peak temperatures and cleavage fracture planes has been discovered.

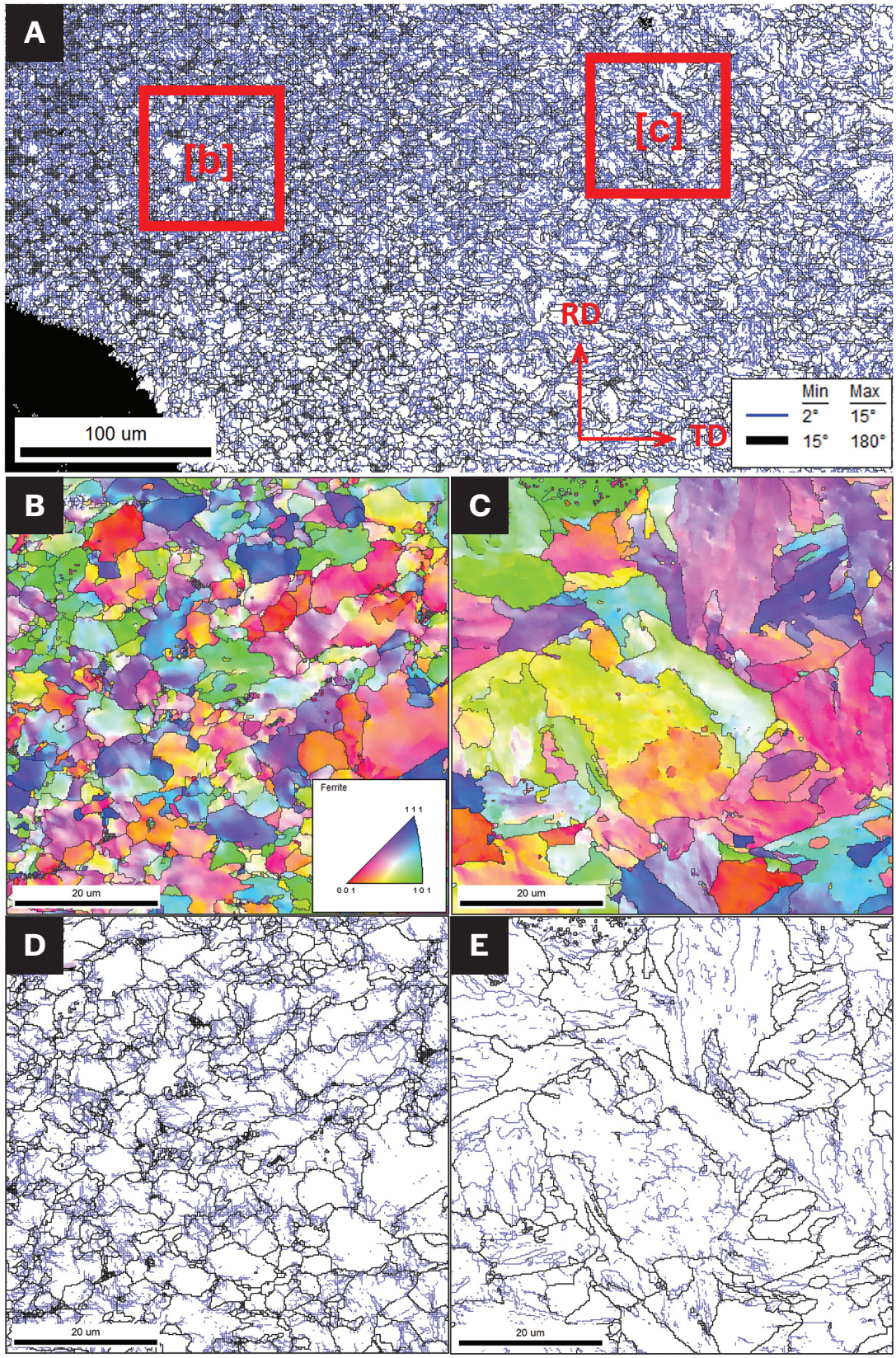

Fig. 10 — A — Grain boundary characteristics adjacent to fracture path for sample PWHTed at 1160°C, and CVN tested at -30°C; B and D — high magnification IPF image of the fracture, which is along the bondline, and corresponding grain boundary characteristics; C and E — are high magnification IPF image of the HAZ and corresponding grain boundary characteristics.

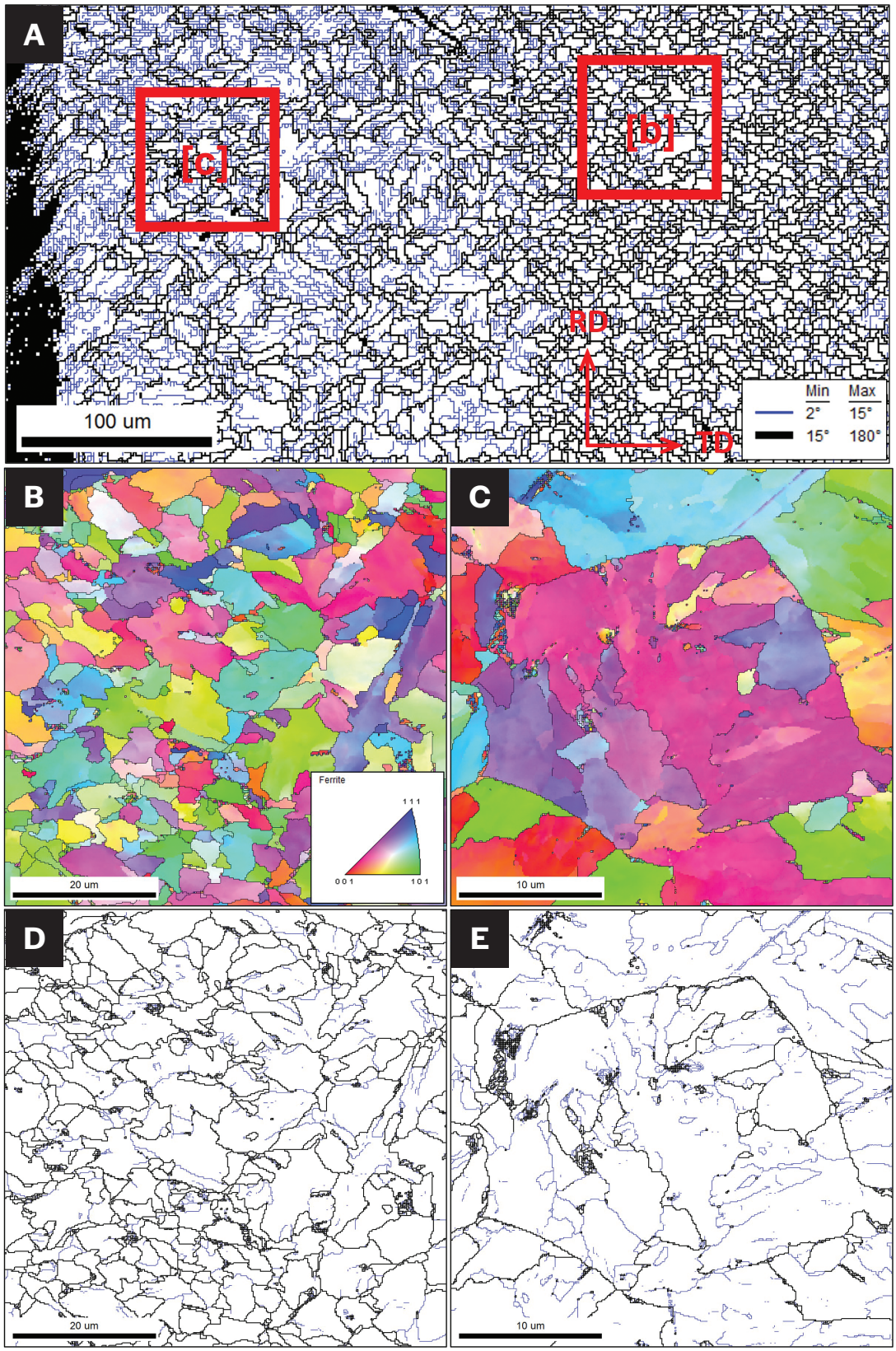

Fig. 11 — A — Grain boundary characteristics adjacent to fracture path for sample PWHTed at 1200°C, and CVN tested at –30°C; B and D — high magnification IPF image of the bondline and corresponding grain boundary characteristics. C and E — high magnification IPF image of the fracture, which is along the HAZ, and corresponding grain boundary characteristics.

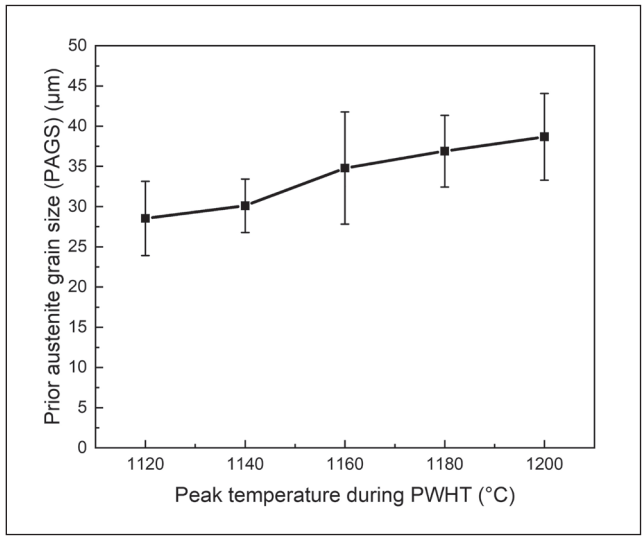

Fig. 12 — Prior austenite grain size (PAGS) for the HAZ as a function of PWHT peak temperature.

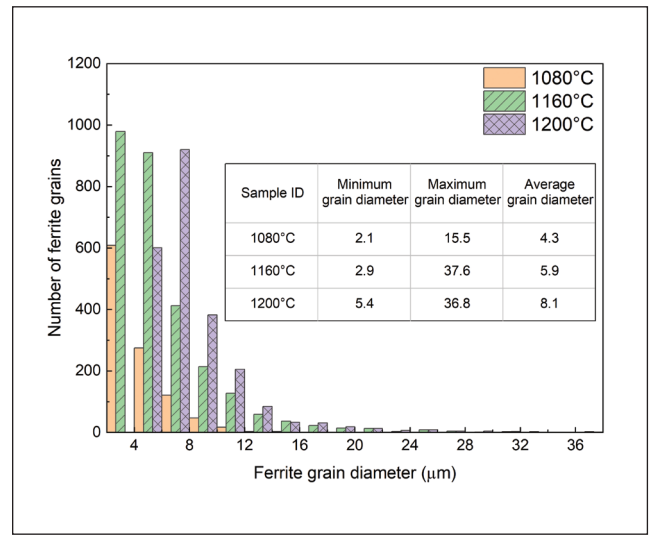

Fig. 13 — Ferrite grain size distribution in the HAZ for specimens PWHTed at 1080°C, 1160°C, and 1200°C.

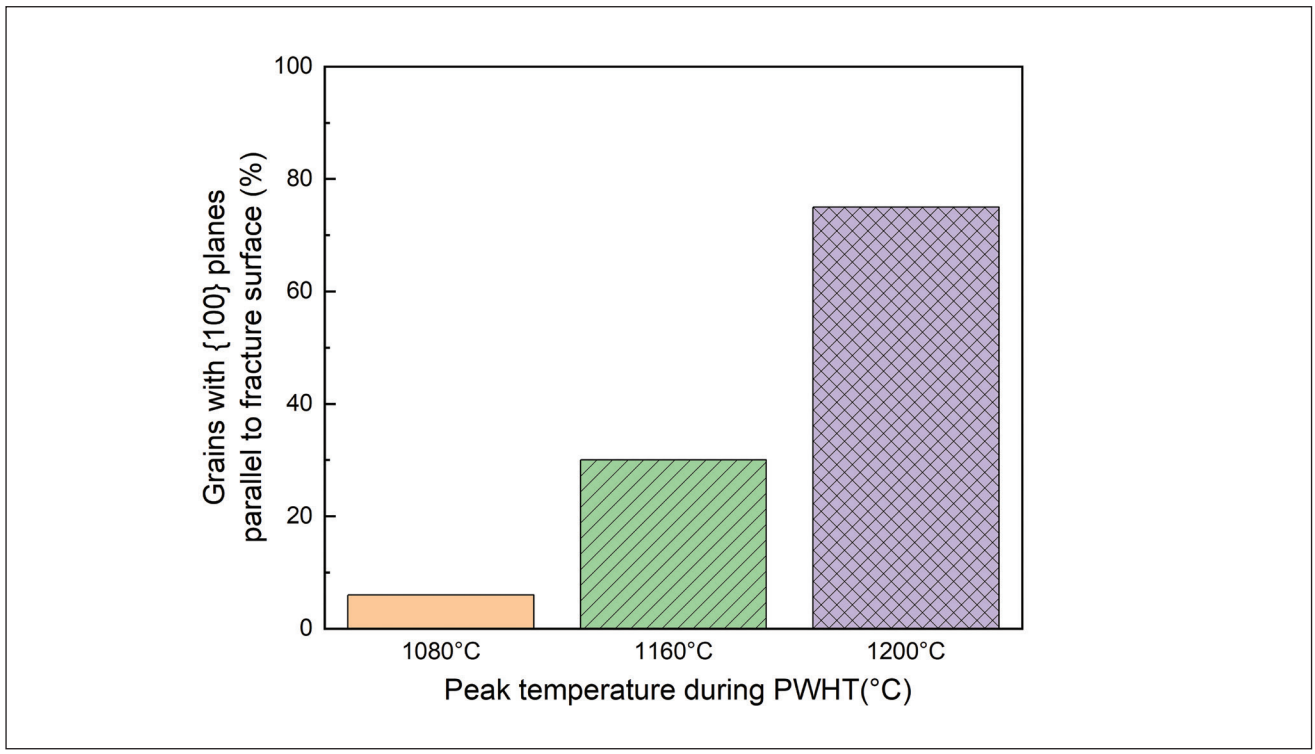

Fig. 14— Area percentage of grains in the HAZ that have {100} planes within 10 deg to the macroscopic fracture plane as a function of PWHT peak temperature.

Discussion

The representative microstructure of the samples PWHTed at 1080°C, 1160°C, and 1200°C are shown in Fig. 15. The microstructure of the bondline and HAZ in the 1080°C peak temperature sample consists of fine equiaxed ferrite (Figs. 15A and B). When the peak temperature is increased to 1160°C (Figs. 15C and D), bainite starts to form in the HAZ (Fig. 15D); however, the microstructure of the bondline seems unchanged and keeps the fine equiaxed ferrite (Fig. 15C), like the 1080°C sample. When the peak temperature has increased to 1200°C, the microstructure of the HAZ predominantly consists of bainite, as shown in Fig. 15F. However, the microstructure of the bondline remains unchanged as equiaxed ferrite (Fig. 15E). Thus, the microstructure of the HAZ gradually has changed from the equiaxed ferrite to bainitic ferrite, as the peak temperature for PWHT is increased from 1080°C to 1200°C.

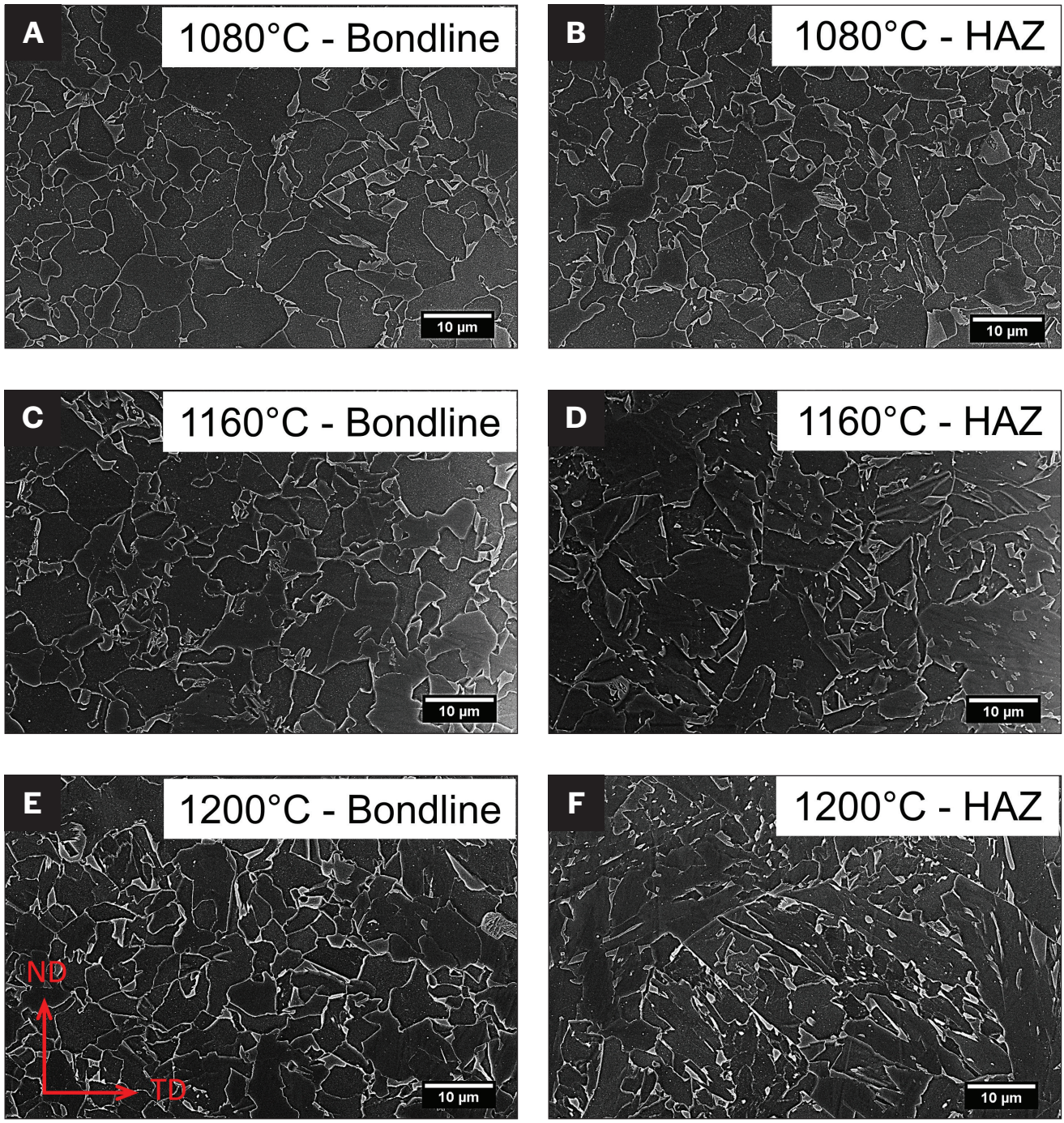

Fig. 15 — Representative in-lens FESEM images of samples PWHTed at peak temperatures of: A — 1080°C bondline; B — 1080°C HAZ; C — 1160°C bondline; D — 1160°C HAZ; E – 1200°C bondline; F — 1200°C HAZ.

For the X70 steel composition in Table 1, the equilibrium phase fraction as a function of temperature is shown in Fig. 15. The inset of Fig. 16 illustrates that in the temperature range 700°C (1292°F) to 1200°C, the phase fraction of the (Ti, Nb) N precipitate keeps at a constant, 0.04 mol, in the steel, which predicts that (Ti, Nb) N would not dissolve into the austenite. However, the Nb (C, N) propitiates completely dissolves at 1200°C. In the temperature change of 1080°C to 1160°C, approximately 50% Nb (C, N) would be dissolved into austenite (Fig. 16). This dissolution of Nb (C, N) has been confirmed in the dilatometry curves, shown in Fig. 16. It must be stressed that the equilibrium calculations from Thermo-Calc cannot accurately predict the non-equilibrium conditions of welding and PWHT. In this study, Thermo-Calc equilibrium results are used to help understand the existence of phases rather than their quantity.

In the derivative of dilation curves, volume changes can be observed above complete austenization, and are attributed to small fractions of Nb (C, N) precipitates being dissolved

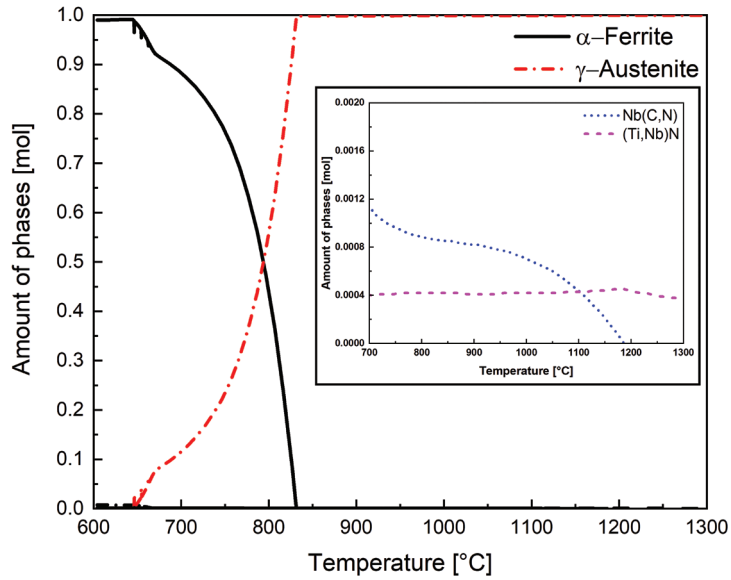

Fig. 16 — Equilibrium phase fraction for all phases as a function of temperature predicted using Thermo-Calc for the X70 steel (inset: magnified view showing Nb (C, N) and (Ti, Nb) N curves).

(Ref. 23). Yan et al. (Ref. 6) also observed this slope change in constant heating rate dilatometry of a similar HF-ERW X65 steel. A similar phenomenon was also observed in austenitic stainless steel during isothermal heat treatments, which dissolved Nb (C, N), with the dilation decreased over time (Ref. 24). Therefore, the deviation in slope, in Fig. 17, after Ac3 is likely due to the diffusion-driven dissolution of Nb (C, N) precipitates (Refs. 22, 24). Therefore, the dissolution and homogenization increase the alloying element levels in austenite. As shown in Fig. 18, as the dissolution of Nb (C, N) precipitate progresses during the PWHT, the concentration of the interstitial element carbon and substitutional element niobium in the solid solution increases as well. Both carbon and niobium can increase hardenability (Ref. 25).

Figure 19A shows the critical phase transformation temperatures on-cooling (Ar3 and Ar1), as measured by dilatometry. It can be observed that as the peak temperature increases from 1080°C to 1200°C, the Ar3 decreases by 96°C (205°F) (707°C to 611°C [1305° to 1132°F]). The decrease in Ar3 temperature can be explained through the theory of hardenability. Prior austenite grain size (PAGS) and chemical composition of austenite can affect the hardenability. At higher peak temperatures, the austenite grain size will increase and therefore increase in hardenability (Fig. 12). Furthermore, increasing the peak temperatures leads to greater solubility of precipitate-forming elements (Nb and Ti-rich second phase, as shown in Fig. 18. It is known that the microalloying elements Nb, Ti, and V are substitutional alloying elements, the radii of which are larger than iron. Nb is the largest, 15.6% larger than iron, with Ti and V being 14.8% and 6.2% larger than iron (Ref. 26). These substitutional alloying elements have lower mobility and can significantly impact reconstructive transformations. Additionally, Nb can also increase hardenability (Ref. 27). Niobium segregates on the austenite grain boundaries, decreasing the interface energy per unit area to make the boundaries less potent nucleation sites for ferrite during austenite to ferrite transformation (Refs. 28, 29). The dissolved alloying elements retard the allotriomorphic ferrite, influence the transformation behavior, and subsequently affect the microstructures in the material. This explains the gradual transition in the microstructure of HAZ from the equiaxed ferrite to bainitic ferrite with the increase in peak temperature during PWHT (Fig. 15). Therefore, it can be summarized that the average grain diameter increases with the increase in austenization temperature. In the current investigation, for the X70 pipeline steel composition, higher peak temperatures during PWHT, such as 1200°C, resulted in the formation of large PAGS due to the dissolution of the Nb-rich second phase and thermal energy provided during PWHT. On cooling, coarse PAG transformed into a coarse bainitic ferrite microstructure at room temperature.

Figure 19B shows that increasing carbon content will lower the phase transformation start temperatures by stabilizing the austenite, leading to the formation of low-temperature microstructures. The number fraction of grain boundary misorientations for the samples PWHTed at 1080°C, 1160°C, and 1200°C are shown in Fig. 20. The sample PWHTed at 1080°C displayed a balanced fraction of high angle grain boundaries (HAGBs), and the low angle grain boundaries (LAGBs) of 42% and 58%, respectively. It was observed that the fraction of HAGBs was highest for the sample PWHTed at 1080°C (42%, Fig. 20A). The samples PWHTed at peak temperatures of 1180°C (32%, Fig. 20B) and 1200°C (26%, Fig. 20C) resulted in the reduction of the HAGBs fraction (misorientation angle > 15) and increase in LAGBs as shown in Fig. 20D. This is attributed to the formation of bainitic ferrite at higher peak temperature (1160°C and 1200°C) PWHT.

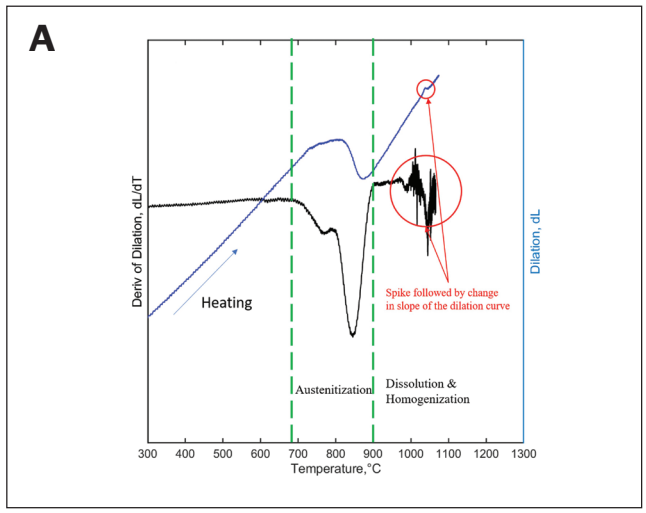

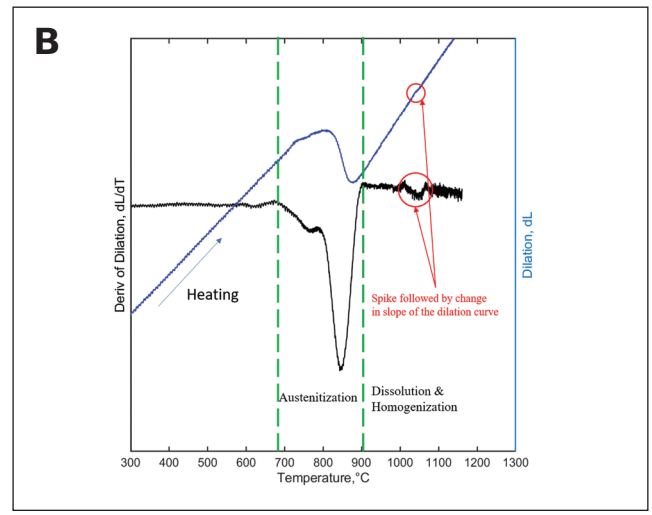

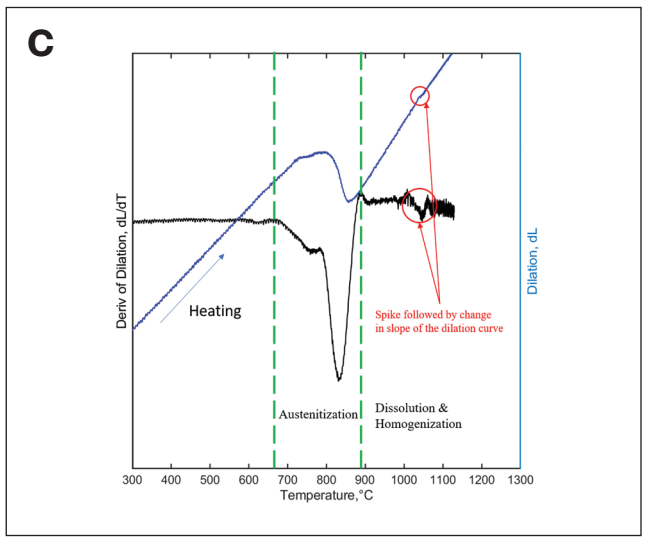

Fig. 17 — Dilatometry analysis of specimens PWHTed at: A — 1080°C; B — 1160°C; C — 1200°C.

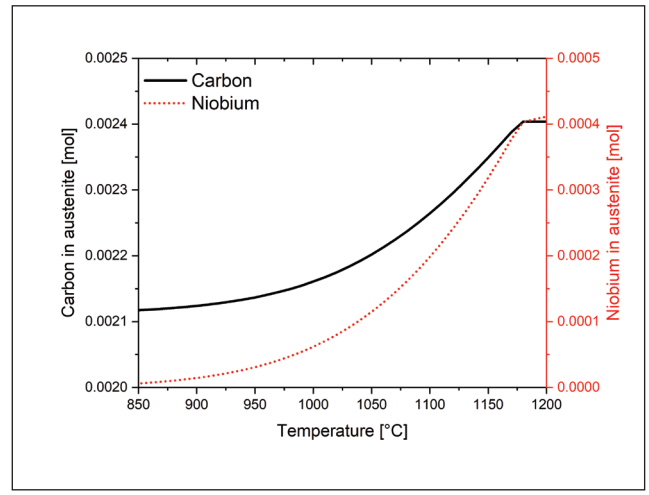

Fig. 18 — Amount of carbon in the austenite (FCC_A1) after A3 temperature as a function of temperature predicted using Thermo-Calc for the X70 steel.

Although the microstructure of the HAZ (Fig. 15) changes significantly with the increase in the PWHT peak temperature, no significant change in the microstructure of the bondline was observed. This is likely due to decarburization/alloy depletion, a commonly observed phenomenon in the HF-ERW welding process (Refs. 12, 13). Based on the differential etching response, it was reported that the carbon concentration in the bondline can be up to 30% lower than in the base metal (Ref. 12). Sharma et al. (Ref. 13) utilized atom probe tomography (APT) to confirm the depletion of carbon and other alloying elements in the bondline ferrite (0.007% C, 1.485% Mn, 0.067% Cr, 0.240% Cu, and 0.188% Si) as compared to the heat-affected zone ferrite (0.015% C, 1.672% Mn, 0.078% Cr, 0.240% Cu, and 0.213% Si). The reduction in the concentration of alloying elements in the bondline reduces the hardenability of this region. Thus, the microstructure of the bondline remains unchanged.

The formation of crystallographic texture has been shown to affect the impact toughness in the HF-ERW pipeline steels (Refs. 8, 10, 11, 16). In the current investigation, with the increase in the peak temperature, an increase in the density of {100} planes that are parallel to the fracture surface is observed (Fig. 14). The density of cleavage planes parallel to the fracture surface is the lowest for the sample PWHTed at 1080°C and highest for 1200°C. The increase in the density of {100} cleavage planes could be due to the increase in the peak temperature during PWHT. The mechanism for the {100} texture formation as a function of heat treatment needs further investigation.

Conclusions

The effect of postweld heat treatment (PWHT) on the impact toughness of a high-frequency electric resistance welded (HF-ERW) X70 pipeline steel has been investigated, and the main conclusions are as follows:

1. The peak temperature for PWHT significantly affects the impact toughness. A significant drop in the toughness values is observed for the specimens PWHTed at peak temperatures of 1180°C and 1200°C, especially for the specimens tested at lower temperatures of –30°C and –45°C.

2. The microstructure of the heat-affected zone (HAZ) gradually has changed from equiaxed ferrite to bainitic fer-

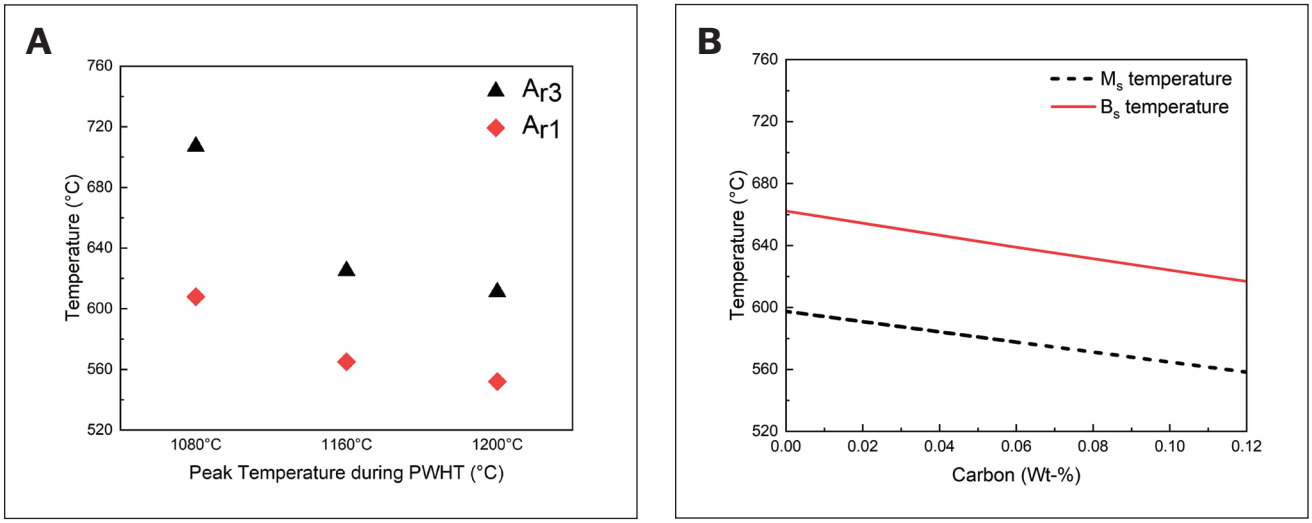

Fig. 19 — A — Phase transformation temperatures during cooling (Ar3 and Ar1), as measured by dilatometry; B — martensitic and bainitic start temperatures predicted from Thermo-Calc.

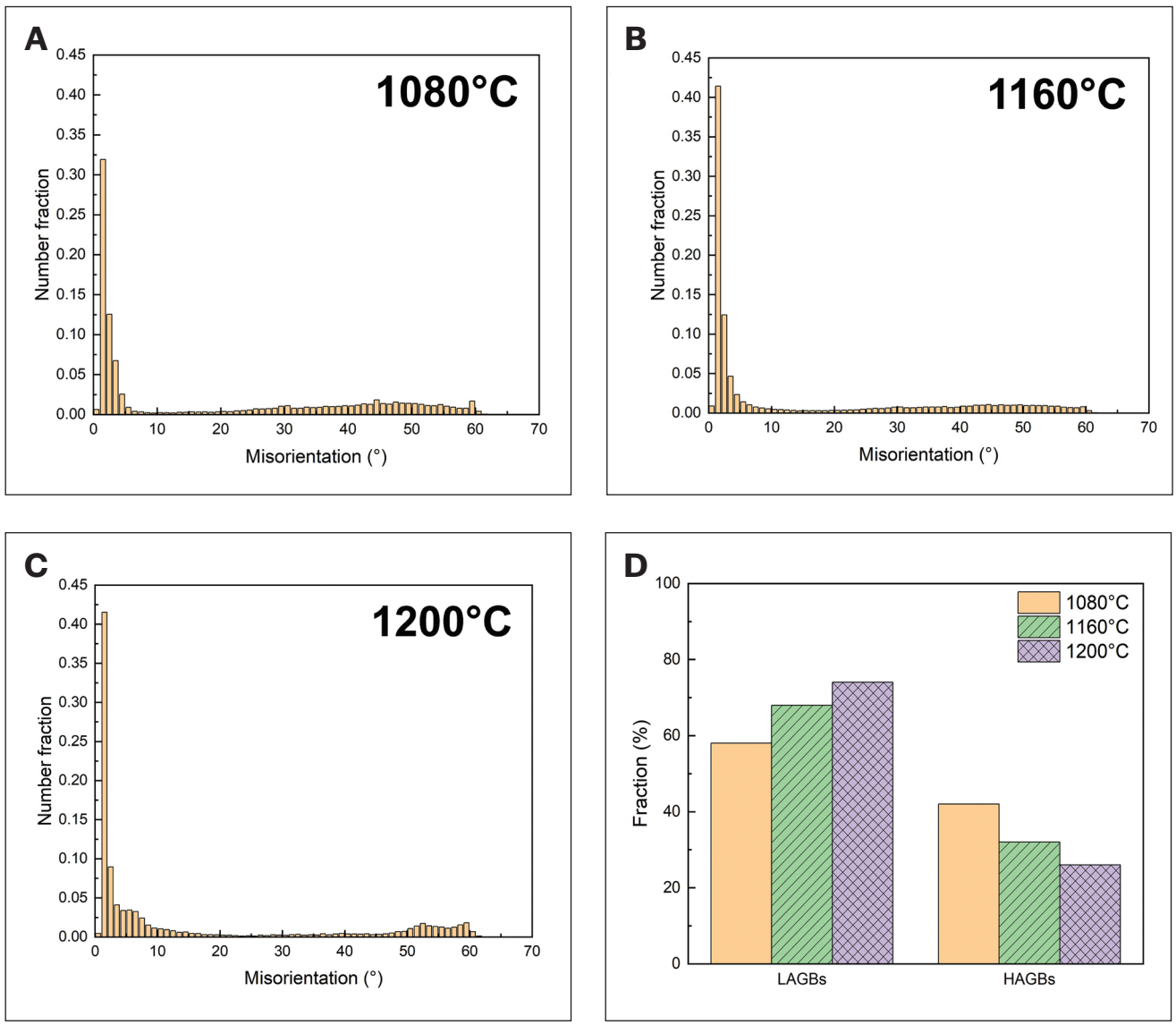

Fig. 20 — Number fraction of grain boundary misorientations in the HAZ for the samples PWHTed at: A — 1080°C; B — 1160°C; C — 1200°C; D — a fraction of low angle grain boundaries (LAGBs, ≤ 15 deg) and high angle grain boundaries (HAGBs, > 15 deg).

rite with the increase in the PWHT peak temperature. There is a reduced fraction of high-angle grain boundaries 248 (HAGBs) in the HAZ at higher peak temperatures. Due to the dissolution of the Nb-rich second phase at temperatures well above the upper critical temperature, a drastic increase in the prior austenite grain size and ferrite grain size is produced at higher peak temperatures.

3. The density of {100} cleavage planes that are within 10 deg of the fracture plane increases with the increase of peak temperature during PWHT. Thus, the increase in the grain size, reduced fraction of HAGBs, and increased fraction of cleavage planes in HAZ may have resulted in poor impact toughness for the HF-ERW X70 post-weld heat-treated at higher peak temperatures.

Acknowledgments

The authors acknowledge the support of the Natural Sciences and Engineering Research Council (NSERC) of Canada through the Collaborative Research and Development (CRD) grant and Mitacs through the Accelerate program.

References

1. Williams, J. G., Killmore, C. R., Barbaro, F. J., Piper, J., and Fletcher, L. 1996. High strength ERW linepipe manufacture in Australia. *Materials Forum* 20: 13–28.

2. Masamura, K., and Nagahama, Y. 2006. Manufacturing processes and products of steel pipes and tubes in JFE steel. *JFE Technical Report* 7(7): 1–6.

3. Kimchi, M. 2011. High-frequency welding. *ASM Handbook* 6A: 456–462.

4. Anderson, N. E. 2018. Influence of the post-weld heat treatment on the low-temperature toughness of ERW API X70 line pipe. MSc thesis, Edmonton, Canada, University of Alberta.

5. Rudnev, V., Loveless, D., and Cook, R. L. 2017. *Handbook of induction heating*, Boca Raton, CRC Press.

6. Yan, P. 2011. High frequency induction welding & post-welding heat treatment of steel pipes. Ph.D. dissertation, Cambridge, UK, University of Cambridge.

7. Kannan, R., Li, L., Guo, L., Anderson, N., Rashid, M., Collins, L., and Arafin, M. 2020. Bond formation mechanism for resistance welding of X70 pipeline steel. *Welding Journal* 99(8): 209s–223s.

8. Yan, P., Güngör, Ö. E., Thibaux, P., Liebeherr, M., and Bhadeshia, H. K. D. H. 2011. Tackling the toughness of steel pipes produced by high frequency induction welding and heat-treatment. *Materials Science and Engineering: A* 528(29–30): 8492–8499.

9. Yan, P., Güngör, Ö. E., Thibaux, P., and Bhadeshia, H. K. D. H. 2010. Crystallographic texture of induction-welded and heat-treated pipeline steel. *Advanced Materials Research* 89: 651–656.

10. Zhang, W., Zhao, G., and Fu, Q. 2018. Study on the effects and mechanisms of induction heat treatment cycles on toughness of high frequency welded pipe welds. *Materials Science and Engineering: A* 736: 276–287.

11. Anijdan, S. M., Aghaie-Khafri, M., Jafarian, H. R., and Khoshakhlagh, A. R. 2018. Role of cube texture on toughness variation of electric resistance welded steel. *Science and Technology of Welding and Joining* 23(5): 387–393.

12. Khalaj, G., Pouraliakbar, H., Jandaghi, M. R., and Gholami, A. 2017. Microalloyed steel welds by HF-ERW technique: Novel PWHT cycles, microstructure evolution and mechanical properties enhancement. *International Journal of Pressure Vessels and Piping* 152: 15–26.

13. Sharma, N. K., Kannan, R., Li, L., Anderson, N., Rashid, M., Collins, L., Poplawsky, J. D., and Unocic, R. 2021. A mechanism for carbon depletion at bondline of high-frequency electric-resistance-welded X70 pipeline steel. *Metallurgical and Materials Transactions A* 52(9): 3788–3798.

14. Kavousi Sisi, A., and Mirsalehi, S. E. 2015. Effect of post-weld heat treatment on microstructure and mechanical properties of X52 linepipe HFIW joints. *Journal of Materials Engineering and Performance* 24(4): 1626–1633.

15. Chung, P. C., Ham, Y., Kim, S., Lim, J., and Lee, C. 2012. Effects of post-weld heat treatment cycles on microstructure and mechanical properties of electric resistance welded pipe welds. *Materials & Design* 34: 685-690.

16. Anijdan, S. M., Aghaie-Khafri, M., Khoshakhlagh, A. R., Eivani, A. R., Park, N., and Jafarian, H. R. 2021. A significant toughness enhancement, and microstructural evolution of an electric resistance welded (ERW) microalloyed steel. *Journal of Materials Research and Technology* 15: 5776–5786.

17. Su, X., Laver, A., Gianetto, J., Liang, J., Tyson, W. R., and Matsuno, S. 2017. Charpy toughness of ERW seam welds. *Journal of Pipeline Engineering* 16(3): 149–167.

18. ASTM A370-22: 2022. *Standard test methods and definitions for mechanical testing of steel products*. West Conshohocken, PA. ASTM International.

19. ASTM E384-17:2022. *Standard test method for microindentation hardness of materials*. West Conshohocken, PA: ASTM international.

20. Andersson, J. O., Helander, T., Höglund, L., Shi, P., and Sundman, B. 2002. Thermo-Calc & DICTRA, computational tools for materials science. *Calphad* 26(2): 273–312.

21. ASTM A1033-18: 2018. *Standard practice for quantitative measurement and reporting of hypoeutectoid carbon and low-alloy steel phase transformations*. West Conshohocken, PA. ASTM International.

22. Kannan, R., Wang, Y., Bannister, R., Rashid, M., and Li, L. 2018. Homogenisation of austenite during non-equilibrium heating in hypereutectoid steels. *Materials Science and Technology* 34(18): 2271–2286.

23. Chatelier, C. C. 2018. Precipitation analysis in microalloyed X70 steels and heat treated I80 and T95 steels. MSc thesis, Edmonton, Canada, University of Alberta.

24. Li, L., and Messler, R. W. 2000. Stress relaxation study of heat-affected zone reheat cracking in Type 347. *Welding Journal* 79(6):136s–144s.

25. Han, X. L., Wu, D. Y., Min, X. L., Wang, X., Liao, B., and Xiao, F. R. 2016. Influence of post-weld heat treatment on the microstructure, microhardness, and toughness of a weld metal for hot bend. *Metals* 6(4): 75.

26. Hulka, K. 2005. The role of niobium in low carbon bainitic HSLA steel. *1st International Conference on Super-High Strength Steels*. Rome, Italy.

27. Speer, J. G., and Hansen, S. S. 1989. Austenite recrystallization and carbonitride precipitation in niobium microalloyed steels. *Metallurgical Transactions A* 20(1): 25–38.

28. Enomoto, M., Nojiri, N., and Sato, Y. 1994. Effects of vanadium and niobium on the nucleation kinetics of proeutectoid ferrite at austenite grain boundaries in Fe–C and Fe–C–Mn alloys. *Materials Transactions JIM* 35(12): 859–867.

29 Ouchi, C., Sampei, T., and Kozasu, I. 1982. The effect of hot rolling condition and chemical composition on the onset temperature of γ-α transformation after hot rolling. *Transactions of the Iron and Steel Institute of Japan* 22(3): 214–222.

KOPPARTHI RAVIKIRAN, **LEIJUN LI** (*leijun@ualberta.ca*), **SUVAN DEV CHOUDHURY**, and **NITIN SAINI** are with the Department of Chemical and Materials Engineering, University of Alberta, Edmonton, Alberta, Canada. **NITIN KUMAR SHARMA** is with the Department of Metallurgical & Materials Engineering, Indian Institute of Technology – Jodhpur, Rajasthan, India. **NEIL ANDERSON** is with Oak Forensic Engineering Ltd., Calgary, Alberta, Canada . **YIYU (JASON) WANG** is with the Materials Science and Technology Division, Oak Ridge National Laboratory. Knoxville, Tenn. **MUHAMMAD RASHID** is with Evraz Inc. NA, Regina, Saskatchewan, Canada.